

## The MIGHTI Wind Retrieval Algorithm: Description and Verification

Brian J. Harding, Jonathan J. Makela,  
Christoph R. Englert, Kenneth D. Marr,  
John M. Harlander, Scott L. England,  
Thomas J. Immel

Received: 18 October 2016 / Accepted: 25 March 2017  
© Springer Science+Business Media Dordrecht

**Abstract** We present an algorithm to retrieve thermospheric wind profiles from measurements by the Michelson Interferometer for Global High-resolution Thermospheric Imaging (MIGHTI) instrument on NASA's Ionospheric Connection Explorer (ICON) mission. MIGHTI measures interferometric limb images of the green and red atomic oxygen emissions at 557.7 nm and 630.0 nm, spanning 90-300 km. The Doppler shift of these emissions represents a remote measurement of the wind at the tangent point of the line of sight. Here we describe the algorithm which uses these images to retrieve altitude profiles of the line-of-sight wind. By combining the measurements from two MIGHTI sensors with perpendicular lines of sight, both components of the vector horizontal wind are retrieved. A comprehensive truth model simulation that is based on TIME-GCM winds and various airglow models is used to determine the accuracy and precision of the MIGHTI data product. Accuracy is limited primarily by spherical asymmetry of the atmosphere over the

---

B.J. Harding  
Department of Electrical and Computer Engineering, University of Illinois at Urbana-Champaign, Urbana, IL, USA  
E-mail: bhardin2@illinois.edu

J. J. Makela  
Department of Electrical and Computer Engineering, University of Illinois at Urbana-Champaign, Urbana, IL, USA  
E-mail: jmakela@illinois.edu

C. R. Englert  
Space Science Division, Naval Research Laboratory, Washington, D.C., USA

K. D. Marr  
Space Science Division, Naval Research Laboratory, Washington, D.C., USA

J. M. Harlander  
Department of Physics, Astronomy and Engineering Science, St. Cloud State University, St. Cloud, MN, USA

S. L. England  
Space Sciences Laboratory, University of California Berkeley, Berkeley, CA, USA

T. J. Immel  
Space Sciences Laboratory, University of California Berkeley, Berkeley, CA, USA

spatial scale of the limb observation, a fundamental limitation of space-based wind measurements. For 80% of the retrieved wind samples, the accuracy is found to be better than 5.8 m/s (green) and 3.5 m/s (red). As expected, significant errors are found near the day/night boundary and occasionally near the equatorial ionization anomaly, due to significant variations of wind and emission rate along the line of sight. The precision calculation includes pointing uncertainty and shot, read, and dark noise. For average solar minimum conditions, the expected precision meets requirements, ranging from 1.2 to 4.7 m/s.

**Keywords** Thermospheric winds · Limb imaging · Interferometry · Inverse theory

## 1 Background

The Ionospheric Connection Explorer (ICON) is a NASA mission designed to study the extreme variability of Earth's ionosphere and identify its drivers, which are thought to originate from both above and below, by the interaction of the solar wind with Earth's magnetosphere, and by meteorological processes in the lower atmosphere [9]. The primary science goals of the ICON mission are to (1) identify what causes the highly-structured variability in the low-latitude quiet-time ionosphere, (2) understand the processes that couple large-scale atmospheric waves to the ionosphere, and (3) determine how these internal drivers compete with external drivers from the sun and geomagnetic activity. One critical measurement needed to achieve these goals is the thermospheric neutral wind.

ICON will remotely sense the thermospheric neutral wind by observing the Doppler shift of two naturally-occurring atomic oxygen airglow emissions, known as the green line (from the  $O(^1S-^1D)$  transition, centered at 557.7 nm) [7, 1] and the red line (from the  $O(^1D-^3P)$  transition, centered at 630.0 nm) [8]. The Doppler shift of these emissions is indicative of the bulk motion of the emitting particles, which is equivalent to the neutral wind under the assumption that the particles have experienced a sufficient number of collisions to thermalize with the ambient neutral gas before emitting.

The instrument that will measure this Doppler shift is the Michelson Interferometer for Global High-resolution Thermospheric Imaging (MIGHTI) [4]. The optical technique used by MIGHTI combines elements from the Wind Imaging Interferometer (WINDII) flown on NASA's Upper Atmosphere Research Satellite (UARS) mission [21] and the Spatial Heterodyne Imager for Mesospheric Radicals (SHIMMER) on STPSat-1 [5]. The limb scene observed by MIGHTI is imaged onto a CCD (Charge Coupled Device) through an interferometer, which superimposes a fringe pattern onto the scene. The phase of the fringe pattern relates to the line-of-sight wind and the amplitude relates to the emission rate. The red and green interferogram images are simultaneously recorded on separate parts of the CCD, to be treated independently. The field of view spans the altitude range 90-300 km for green and 150-300 km for red. During the day, the green emission will be used to determine the altitude profile of the winds below 170 km, and the red will be used above 170 km. At night, the narrowing of the atmospheric emission profiles will limit measurements to the range 90-105 km (green) and 210-300 km (red). The native altitude sampling of MIGHTI is about 2.5 km, although we expect to

bin to 5 km for green and to 30 km for red to improve statistics while meeting the ICON science requirements [9]. As with all limb observations, the MIGHTI measurements are averages (weighted by the airglow emission rate) along the horizontal region spanned by the line of sight (many hundreds of km), the vertical sampling (natively 2.5 km), and the exposure time (30 or 60 seconds, which carries the spacecraft 250 or 500 km horizontally). This limits MIGHTI's ability to detect small-scale waves. MIGHTI also measures brightness profiles of the  $O_2$  A-band spectrum using three spectrally narrow in-band and two background channels in the altitude range 90-140 km to retrieve the thermospheric temperature [22].

Using only one of the two identical MIGHTI sensors, only one of the two components of the vector horizontal wind are measured. To determine both components, data from both MIGHTI sensors, denoted MIGHTI A and B, are used which have lines of sight offset by  $\sim 90$  degrees. Both sensors observe to the side of the spacecraft, with MIGHTI A's line of sight at an azimuthal angle of  $\sim 45^\circ$  relative to the spacecraft velocity vector, and MIGHTI B's line of sight at an azimuthal angle of  $\sim 135^\circ$  to the spacecraft velocity vector.

The raw interferogram image recorded by MIGHTI contains a number of artifacts caused by thermal drift, flat-field variations, fringe modulation efficiency variations, stars, cosmic rays, and calibration lamps. The first step in processing a MIGHTI image removes these artifacts to generate a calibrated interferogram image, known as the MIGHTI Level 1 data product [4].

The purpose of this paper is to describe the algorithm that retrieves vector wind profiles from a time series of calibrated interferogram images. In Section 2, we describe the first step in this algorithm, which unravels the line-of-sight integration to retrieve an altitude profile of one component of the horizontal wind, known as the MIGHTI Level 2.1 data product. Section 3 presents the second step of this algorithm, which combines observations from MIGHTI A and B to derive altitude profiles of the vector horizontal wind, the MIGHTI Level 2.2 data product. In Section 4, this algorithm is tested with a simulation of a full orbit of MIGHTI observations to determine under what conditions the MIGHTI data product is expected to be accurate, given realistic airglow, wind, and temperature distributions. We also characterize the expected precision. Section 5 presents conclusions and describes future work.

## 2 Line-of-sight wind retrieval

In this section, we describe how a calibrated MIGHTI interferogram image (the MIGHTI Level 1 data product) is analyzed to retrieve an altitude profile of the line-of-sight component of the horizontal wind (the MIGHTI Level 2.1 data product). A simulated example of a calibrated MIGHTI interferogram image of the green line is shown in the left panel of Figure 1. The vertical axis contains altitude information, and the horizontal axis contains spectral information, as points along the horizontal axis of the CCD sample the fringe pattern corresponding to a varying optical path difference across the aperture. We are interested in recovering the variation of wind in the vertical direction, which manifests as slight changes in the phase of the interferogram. We begin by describing the relationship between the wind and the phase in a single row of the interferogram, and then proceed to detail the inversion of the full interferogram image to retrieve an altitude profile of the wind,

followed by a discussion of a calibration procedure to determine the fringe phase corresponding to zero wind (i.e., pure corotation of the atmosphere).

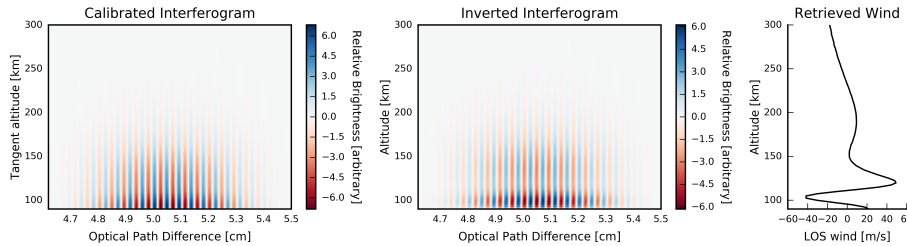


**Fig. 1** (Left) The real part of a simulated green line MIGHTI Level 1 data product, a calibrated interferogram image, without noise. (Middle) The same interferogram image, inverted with the algorithm in Section 2.2. This inversion reveals two distinct maxima in the brightness vs. altitude profile, and a drastic phase shift at 100 km. (Right) The line-of-sight (LOS) wind profile extracted from the inverted interferogram image.

## 2.1 The relationship between phase and wind

A single row of the calibrated interferogram is denoted  $I(x)$ . The independent variable,  $x$ , is the position along the horizontal axis of the detector, which is related to the optical path difference. The calibrated interferogram is provided as an amplitude and phase at each binned pixel location on the detector, which we treat as a complex quantity. Note that the raw, observed interferogram is of course purely real, but the calibration process transforms it to a complex quantity. The relationship between  $I(x)$  and the observed spectrum is [4]:

$$I(x) = \int_0^{\infty} B(\kappa) e^{j[2\pi\kappa x + \Theta(\kappa, x)]} d\kappa \quad (1)$$

where  $\kappa$  is proportional to the difference between the wavenumber and the Littrow wavenumber of the interferometer,  $B(\kappa)$  is the observed spectral density,  $\Theta$  is a phase distortion term, and constant factors have been omitted for simplicity. Since the Level 1 processing removes the  $x$ -dependence of  $\Theta$ , and the  $\kappa$ -dependence is negligible over the support of  $B(\kappa)$ , we can regard  $\Theta$  as a scalar to be determined as part of the zero-wind phase calibration (See Section 2.3). We have omitted terms relating to spatial and spectral variations in transmittance and fringe modulation efficiency, since these are removed in the Level 1 processing. In practice, the bounds of the integral are limited by the optical filter and the Level 1 processing to include only the emission of interest. We assume that there is negligible variation of  $B(\kappa)$  across the horizontal field of view of  $\sim 3.2^\circ$  [4]. The Level 1 calibration has removed the phase error and the DC value (i.e., non-modulated term) from  $I(x)$ . The magnitude reduction at the edges of the image in Figure 1 is because apodization has been applied to limit edge effects in the interferogram processing. This does not affect the phase measurement.

An important consequence of Eq. (1) is that a Doppler shift in the spectrum,  $B(\kappa)$ , manifests as a phase shift in the interferogram,  $I(x)$ . This can be easily

understood from the approximate Fourier transform relationship between  $B(\kappa)$  and  $I(x)$ : a small shift in a monochromatic line  $B(\kappa)$  yields a small change in fringe frequency in the interferogram. At large path differences, this small frequency shift manifests as a cumulative phase shift. The relationship between the phase shift and the Doppler velocity is [3]:

$$\Delta\phi = \frac{2\pi d}{\lambda c} v \quad (2)$$

where  $\Delta\phi$  is the phase shift in  $I$  when observing a line-of-sight wind speed  $v$ , defined as positive towards MIGHTI,  $c$  is the speed of light,  $\lambda$  is the rest wavelength of the emission, and  $d$  is the optical path difference. The phase shift is ideally a linear function of  $d$ , and the average phase shift over the measured path interval can be used to retrieve the Doppler shift. The contribution of the spacecraft velocity to the Doppler shift depends on  $x$  and the row, as discussed in the next section.

The phase measurement corresponding to zero wind speed – known as the zero-wind phase,  $\phi_z$  – is not known and must be determined through calibration, described in Section 2.3. Once the zero-wind phase is known, it is removed from the phase measurement to obtain  $\Delta\phi$ , which can be used in Eq. (2) to determine the line-of-sight wind:

$$\Delta\phi = \phi - \phi_z \quad (3)$$

## 2.2 Inverting an interferogram image

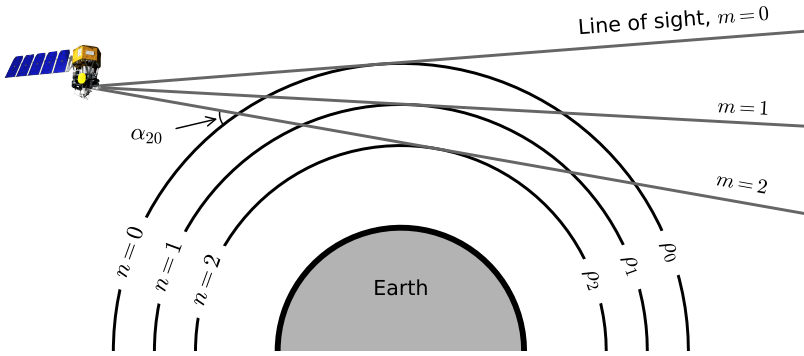


**Fig. 2** Observation geometry for a MIGHTI interferogram (not to scale). The angle between the  $m^{\text{th}}$  line of sight and the horizontal plane at the intersection with the  $n^{\text{th}}$  layer is  $\alpha_{mn}$ . Each altitude layer is assumed to be represented by atmospheric parameters,  $\rho_n$ : wind speed, temperature, and volume emission rate, which are assumed to be independent of latitude and longitude (spherical symmetry assumption). In practice,  $\sim 90$  lines of sight and altitude layers are used.

In an actual observation, each row of the interferogram contains contributions from many different layers of Earth's atmosphere, each characterized by a different wind, temperature, and volume emission rate, as shown in Figure 2. It is thus not appropriate to use the simple formulation described in the previous section, in which the measured phase shift corresponds to a single wind speed. Instead, we must explicitly include the line-of-sight integration in our formulation, which we will later invert to retrieve the wind as a function of altitude. We start by formulating the model for a single line of sight and will later generalize to all lines of sight. The spectrum observed by the field of view of the  $m^{\text{th}}$  row of MIGHTY's CCD is denoted  $B_m^{\text{obs}}(\kappa)$  and can be written as an integral along that row's line of sight:

$$B_m^{\text{obs}}(\kappa) = \int_0^\infty B(\kappa - \Delta\kappa, h) ds \quad (4)$$

where  $B(\kappa, h)$  describes the spectrum at altitude  $h$  in the absence of a Doppler shift,  $\Delta\kappa$  is the Doppler shift induced by the altitude-dependent line-of-sight wind, and it is assumed that all atmospheric quantities are spherically symmetric, i.e., they have negligible dependence on latitude and longitude over the region being observed. We discretize this problem by treating the spectra at the tangent altitudes as the unknowns, and by approximating the integral in Eq. (4) as a summation:

$$B_m^{\text{obs}}(\kappa) = \sum_{n=0}^{N-1} B_n(\kappa - \Delta\kappa_{mn}) w_{mn} \quad (5)$$

where  $N$  is the number of altitude layers, the function  $B_n(\kappa)$  describes the unknown spectrum at altitude  $n$  in the absence of a Doppler shift,  $\Delta\kappa_{mn}$  is the Doppler shift induced by the line-of-sight component of the wind at altitude  $n$  for the line of sight  $m$ , and  $w_{mn}$  is a weight determined by the summation rule used to approximate the integral. In this work, we use a zero-order (i.e., Riemann sum) rule, but higher order rules can be used to improve accuracy at the cost of precision. For the rare cases when there is significant red-line emission above the highest observed altitude of 300 km, it is important how the contributions from above 300 km are handled in the integral. Instead of assuming the airglow emission rate goes immediately to zero above 300 km, we assume it decays exponentially following a scale height of 26 km (a value extracted from the models described in Section 4). Incorporating this assumption simply requires adding an extra term to  $w_{m0}$ , denoted  $w_{m0}^{\text{above}}$ :

$$w_{m0}^{\text{above}} = \int_{\sqrt{r_0^2 - r_m^2}}^\infty e^{-\frac{1}{H}(\sqrt{x^2 + r_m^2} - r_0)} dx \quad (6)$$

where  $H = 26$  km,  $r_m$  is the radial distance from the center of the Earth to the tangent altitude of line of sight  $m$ ,  $r_0 = R_E + 300$  km,  $R_E$  is the radius of Earth, and the integral is evaluated numerically.

Using Eq. (5) in Eq. (1) and switching the order of integration yields a model for the integrated interferogram, which we denote  $H_m(x)$ :

$$H_m(x) = \sum_{n=0}^{N-1} \left( \int_0^\infty B_n(\kappa - \Delta\kappa_{mn}) e^{j[2\pi\kappa x + \Theta(\kappa)]} d\kappa \right) w_{mn} \quad (7)$$

If  $\Delta\kappa_{mn}$  were zero (i.e., no wind in the atmosphere), we could use Eq. (1) to replace the term in parentheses with the interferogram  $I_n(x)$ . However, the wind in layer  $n$  creates a Doppler shift, so  $\Delta\kappa_{mn}$  is not zero. Following the discussion in Section 2.1, this causes a phase shift in  $I_n(x)$ . If we let  $\Delta\phi_n$  denote the phase shift caused by the horizontal wind within layer  $n$  in the plane of Figure 2, then  $\Delta\phi_n \cos \alpha_{mn}$  is the phase shift caused by the line-of-sight wind component in layer  $n$ , where  $\alpha_{mn}$  is the angle between the line of sight and the direction parallel to the ground, as shown in Figure 2. This assumes the vertical wind is zero, and our simulations using realistic 3D wind and emission profiles show that the error introduced by this assumption is negligible in comparison to other sources of error. This substitution yields a complete model for the MIGHTI observation, if we let  $m$  run from 0 (the top row of the interferogram) to  $M - 1$  (the bottom row):

$$H_m(x) = \sum_{n=0}^m I_n(x) e^{j\Delta\phi_n \cos \alpha_{mn}} w_{mn} \quad \forall m \in [0, M - 1] \quad (8)$$

The unknowns in this equation are  $\Delta\phi_n$ , related to the wind in each layer, and  $I_n(x)$ , related to the volume emission rate and emission line shape in each layer. By construction, the number of altitudes,  $N$ , is equal to the number of measurements,  $M$ , and is approximately 90 in practice. The nonlinear system of equations in Eq. (8) has a unique solution which can be obtained by a process similar to backsubstitution, commonly known as ‘‘onion-peeling.’’ Intuitively, the idea is that the properties at the top altitude can be obtained directly from the top measurement, since no other altitudes contribute. Then, the contributions of the top altitude to the second measurement are removed from the second measurement, and so on. Mathematically, this retrieval can be written:

$$\begin{aligned} I_0(x) e^{j\Delta\phi_0} &= \frac{1}{w_{00}} H_0(x) \\ I_m(x) e^{j\Delta\phi_m} &= \frac{1}{w_{mm}} \left( H_m(x) - \sum_{n=0}^{m-1} I_n(x) e^{j\Delta\phi_n \cos \alpha_{mn}} w_{mn} \right) \quad \forall m \in [1, M - 1] \end{aligned} \quad (9)$$

where we have used the fact that  $\alpha_{mm} = 0$ . The inversion proceeds iteratively, starting with  $m = 0$ . At each step  $m$ , Eq. (9) describes a row of the interferogram containing information solely from altitude  $m$ . The phase shift,  $\Delta\phi_m$ , and thus the line-of-sight wind speed, are extracted using the process described in Section 2.1. An inverted interferogram and line-of-sight wind profile are shown in Figure 1.

This retrieval assumes all quantities are described in an inertial reference frame. In practice, the MIGHTI interferogram is recorded in the spacecraft frame. Thus, before the retrieval, the projected spacecraft velocity is removed from the interferogram by subtracting the appropriate phase given by Eq. (2) from each pixel in the image. Even though the field of view is only a few degrees, the horizontal and vertical variation of this projected velocity within the image is significant and is taken into account. After retrieving the line-of-sight wind as described above in an inertial frame, we transform to an Earth-fixed frame by removing the contribution of Earth’s rotation at each altitude.

Uncertainties in the Level 1 data product are provided as an amplitude and phase uncertainty per row of the calibrated interferogram. These uncertainties are propagated through the retrieval described above to generate uncertainties in the line-of-sight wind. An uncertainty is added in quadrature to account for errors in spacecraft velocity removal, which is caused by spacecraft pointing uncertainty. The value of this pointing uncertainty will be determined post-launch and is expected to be around 1 m/s.

The Level 2.1 data product contains the retrieved line-of-sight wind profile with uncertainty, the location (latitude, longitude, and altitude) of each point in the wind profile, the azimuth angle of the line of sight at the tangent point, and other ancillary information. In the normal operating modes, there is one Level 2.1 data product per MIGHTI sensor, per emission line, per exposure.

The WINDII instrument on the UARS mission was in many ways similar to MIGHTI, having observed the same emission lines with a Michelson interferometer [21]. It is worthwhile to point out the major conceptual differences between the inversion used for WINDII and the inversion for MIGHTI. The WINDII analysis made use of “apparent quantities” which were related to effective wind, temperature, and emission rate of individual rows of the integrated interferogram before inversion, contrasting with the MIGHTI inversion which retrieves these quantities after the inversion. For WINDII, the order did not matter, since the WINDII instrument stepped over a small range of optical path differences, representing one fringe. Over this small range, it can be assumed that the magnitude of  $I(x)$  does not vary with  $x$ . For MIGHTI, this assumption cannot be made, so the order is important. Additionally, the WINDII inversion neglected the  $\cos \alpha$  term in Eq. (8), finding that the resulting error was only 3%, which was negligible compared to other error sources [19]. This allowed the use of a linear inversion. For the expected performance of MIGHTI, neglecting this term can yield errors in excess of random measurement error, justifying the use of a nonlinear inversion.

The use of a linear inversion made it straightforward for WINDII to implement a regularized inversion [20,6]. Regularization has the benefit of suppressing noise effects such as retrieval oscillations and recovering smoother wind profiles. However, the costs of regularization are systematic errors such as bias [14]. If many observations of the same, unregularized wind profile are averaged together, the noise will converge to zero, and the average will converge to the true wind profile. This is not true if a regularized inversion is used; the average will be smoother than the true wind profile. One of the primary ICON science goals will be achieved by averaging many wind profiles to quantify tidal amplitudes. The standard MIGHTI data product is not regularized, so that these tidal amplitudes will not be biased. For other purposes, for example at the higher altitudes in the MIGHTI FOV, where strong wind shears are expected to be suppressed due to the increasing atmospheric viscosity, a regularized inversion may be desired, but it has not yet been implemented.

### 2.3 Zero-Wind Phase Calibration

The accuracy of the retrieved wind profile depends on the knowledge of  $\phi_z$ , the zero-wind phase, the phase measured by the interferometer at the rest wavelength of the emission. Since there are no suitable oxygen lamps that produce the ther-

atmospheric target emissions at 630.0 nm and 557.7 nm for on-board calibration,  $\phi_z$  will be determined by yawing the spacecraft so that the instrument observes the same region of the atmosphere from opposite directions (ram and wake) within a short period of time, a procedure known as the zero-wind maneuver. There are separate zero-wind maneuvers for MIGHTI A and for MIGHTI B.

First, the spacecraft rotates so that one of the MIGHTI sensors' line of sight has an azimuth component matching that of the spacecraft velocity. This position is held while MIGHTI takes an image. Next, the spacecraft rotates 180° and the same MIGHTI sensor takes another image. These images are taken roughly 10 minutes apart, and are timed so that the same region of the atmosphere is being observed. It is assumed that the wind field does not change significantly over this time.

The zero wind maneuver images are processed with the algorithm described above to obtain two wind profiles. If the value of  $\phi_z$  is correct, and noise is negligible, then these two wind profiles should add to zero. Since  $\phi_z$  is not known, it is iterated until the sum of the two profiles is minimized. Simulations have determined that the zero wind maneuver will recover  $\phi_z$  with an accuracy equivalent to a 1 m/s wind. There will be a different value of  $\phi_z$  for each of the emissions being observed and each of the MIGHTI sensors in day and night mode. To assess and quantify the potential drift of the zero wind phase, we plan to perform this zero wind calibration once per month per instrument. Fringe drifts associated with changes in the sensor's thermal environment will occur on much shorter time scales and will be removed with the aid of measurements of on-board calibration lamps in Level 1 processing. The on-board calibration lamps produce neon and krypton emission lines with wavelengths that are fractions of a nanometer different from the observed atmospheric lines. This allows the measurements of thermal drifts simultaneously to the atmospheric observations. Calibration lamps are going to be used for one orbit every 24 hour day [4].

### 3 Cardinal wind retrieval

In this section, we describe the process by which the line-of-sight wind measurements from the two MIGHTI sensors (the MIGHTI Level 2.1 data product) are combined to retrieve the cardinal wind, i.e., the zonal and meridional components (the MIGHTI Level 2.2 data product). The observation geometry is shown in Figure 3. First, MIGHTI A measures a wind component along its line of sight. Five to eight minutes later, depending on tangent point altitude, the spacecraft has moved to a position such that MIGHTI B measures a nearly orthogonal wind component at approximately the same location. It is assumed that the wind has not changed significantly in this time. Combining these line-of-sight components to retrieve the horizontal wind vector is simply a coordinate transformation:

$$\begin{bmatrix} v_{\text{zonal}} \\ v_{\text{meridional}} \end{bmatrix} = \begin{bmatrix} \sin \gamma_A & \cos \gamma_A \\ \sin \gamma_B & \cos \gamma_B \end{bmatrix}^{-1} \begin{bmatrix} -v_{\text{LOS},A} \\ -v_{\text{LOS},B} \end{bmatrix} \quad (10)$$

where  $v_{\text{zonal}}$  is the retrieved zonal wind, defined as positive eastward,  $v_{\text{meridional}}$  is the retrieved meridional wind, defined as positive northward,  $v_{\text{LOS},A}$  and  $v_{\text{LOS},B}$  are the line-of-sight wind components from MIGHTI A and B, defined as positive

toward MIGHTI, and  $\gamma_A$  and  $\gamma_B$  are the azimuth angles of MIGHTI's lines of sight, shown in Figure 3.

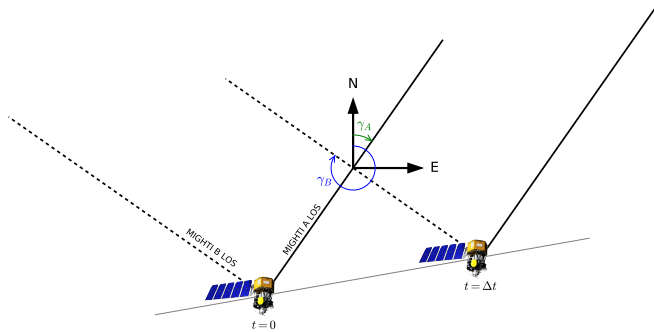


**Fig. 3** Observation geometry for the MIGHTI Level 2.2 cardinal wind retrieval. A line-of-sight (LOS) wind component from MIGHTI A (solid) and a LOS wind component from MIGHTI B (dashed), separated in time, are combined to retrieve zonal and meridional wind components.

Because MIGHTI A and B are continuously taking measurements at a 30-s or 60-s cadence, and since the Earth rotates during the several minutes between MIGHTI A and B observations of the same volume, the tangent points of MIGHTI A and B will never exactly match. Moreover, even if they match closely at one altitude, they will not match at other altitudes for the same two exposures. For these reasons, we interpolate the series of line-of-sight wind profiles to a common, regular grid before using Eq. (10). In practice, we use bilinear interpolation horizontally and vertically for each sensor.

Due to the coupled nature of the algorithm described above, the Level 2.2 data product is generated for an entire orbit simultaneously. The data product contains the reconstruction grid (latitudes, longitudes, and altitudes), the estimated zonal and meridional wind at each grid point with uncertainties, and other ancillary information. There is one Level 2.2 data product per emission line per orbit.

#### 4 Verification

In this section, we present the results of the pre-launch MIGHTI wind verification effort. The intent is to verify that the MIGHTI hardware design and retrieval algorithms satisfy the science requirements of the mission. We also quantify the expected accuracy and precision. The precision calculation includes shot, read, and dark noise, and utilizes realistic airglow emission rates and expected instrument parameters, as discussed below. The accuracy is dominated by spherical asymmetry of the wind and airglow emission rate, causing a systematic error which is inherent to all limb imagers. To quantify the effect of this asymmetry, we simulate a MIGHTI image using realistic, three-dimensional atmospheric parameters and apply the Level 1, Level 2.1 and Level 2.2 algorithms on the simulated image

to derive a cardinal wind profile, which we compare to the wind from the simulated atmosphere. To test the robustness of the MIGHTI data product, we run this simulation as a function of time, spanning a full ICON orbit. A schematic representation of this process is shown in Figure 4.

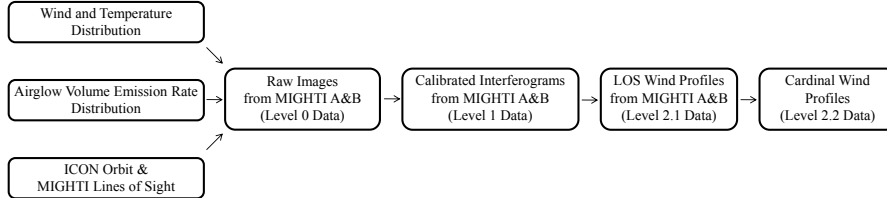


**Fig. 4** Block diagram of the MIGHTI wind verification effort. A time series of simulated MIGHTI observations are fed through the analysis pipeline, and the resulting wind profiles are compared with the winds used in the simulation.

We start with three-dimensional wind and temperature distributions from the Thermosphere-Ionosphere-Mesosphere-Electrodynamics General Circulation Model (TIME-GCM) [18, 17]. This model provides a global, self-consistent, physics-based representation of the circulation, temperature, composition, and electrodynamics of the upper atmosphere and ionosphere, using fixed pressure levels that cover  $\sim 30$  km to  $\sim 500$  km (depending on atmospheric conditions). We use various models for the airglow emission rate. On the dayside, we use empirical climatological models derived from WINDII/UARS data for the red and green emissions [24, 25]. For the nightside, we use photochemical emission models [11–13, 15, 23] informed by NRLMSISE-00 neutral densities and temperatures [16] and IRI-2007 ion densities and temperature [2]. Of particular importance is the terminator, the boundary between daytime and nighttime. The distribution of airglow near the terminator is not well known, nor is it well characterized in the models used here. In our model, we use the daytime model within the reported range of its applicability (a solar zenith angle below  $104.5^\circ$  for red and  $80^\circ$  for green) and use the nighttime model otherwise. This yields a sharp gradient in the airglow distribution near the day/night boundary which constitutes a worst-case test of the terminator effect on the retrieved winds.

Using these models, we simulate the scene that MIGHTI A and B would observe. Given ICON’s position and attitude, we compute the line of sight for each interferogram row for each MIGHTI sensor for each emission color. Stepping along the line of sight in 5 km increments, we calculate the emission spectrum based on the modeled line-of-sight wind, temperature, and emission rate at each point. We add the spectra along the entire line of sight and use Eq. (1) to calculate the observed interferogram. Repeating this for each row of the image yields the full MIGHTI Level 0 data product. For computational expediency, this process treats all lines of sight as narrow lines, and ignores the volume integration over the region subtended by one row. As time progresses in the simulation, the region of the atmosphere sampled by MIGHTI changes as the spacecraft orbits and the Earth rotates, but we neglect the temporal evolution of the winds simulated in

the TIME-GCM, which is generally small over the 5-8 minutes between the observations made by MIGHTI A and B of the same volume. As such, this simulation does not capture the spatiotemporal ambiguity inherent to observations from a moving platform. The simulation captures the effect of Earth's rotation on the observational geometry and Doppler shifts. We also account for the angle between the line of sight and the local horizontal ( $\alpha_{mm}$  in Eq. (8)).

An instrument model creates Level 0 data using as-built instrument parameters (see right column of Table 3 of [4]). The resulting data product is processed using the Level 1 algorithm [4] to generate the Level 1 data product. The effects of imperfect corrections for thermal drifts, phase distortions, flat fields, stars, etc. are ignored. This Level 1 product is processed with the Level 2.1 and Level 2.2 algorithms described in Sections 2 and 3 to generate estimated profiles of the zonal and meridional wind. We then calculate the retrieval error by comparing these profiles with the TIME-GCM wind, after interpolating the TIME-GCM wind to the retrieval grid.

#### 4.1 Accuracy

We first examine a case in which measurement noise is not included in the simulation of the Level 0 files in order to characterize the accuracy of the retrieval. The results are shown in Figure 5. The top panel shows the simulation domain, including the ICON orbit and the vertically-integrated red volume emission rate (630.0 nm), for context. The four bottom panels show the retrieval error. The top row shows the result using the red emission, and the bottom row shows the green emission. The left and right columns show the zonal and meridional wind error, respectively. The horizontal axis of each plot is time, spanning one full orbital period. The top axis indicates how the longitude of the retrieval grid varies over time. The  $\sim 10$ km-period feature in altitude is an artifact of the large grid size in TIEGCM. We display results only in regions where wind measurements are required by the ICON mission (red day: 170-300 km altitude, red night: 200-300 km, green day: 90-170 km, green night: 90-105 km). However, in practice, we expect to extend this range when the signal strength permits.

The results in Figure 5 suggest that the inherent accuracy of the MIGHTI retrieval is usually better than 10 m/s. Indeed, 80% of the points in Figure 5 have an error less than 3.5 m/s for red and 5.8 m/s for green. The error in the red retrieval is dominated by variations of wind and airglow emission rate along the line of sight. The real atmosphere varies with latitude and longitude, so the assumption of local spherical symmetry, while necessary for the wind retrieval, is not strictly valid. This is a fundamental limitation of the horizontal resolution of limb imagers such as MIGHTI and WINDII. Although the green retrieval is affected by this phenomenon as well, it is also affected by the vertical resolution of MIGHTI, discussed in more detail in the next section. These results emphasize that MIGHTI wind measurements should be interpreted as horizontal and vertical averages and not as point measurements.

Also evident in Figure 5 are large errors near the day-night boundary in the airglow models, at  $\pm 90^\circ$  longitude. As discussed above, the airglow gradients in the model are sharp near this boundary, presenting severe violations of spherical symmetry. As the line of sight crosses this boundary, the retrieval error grows

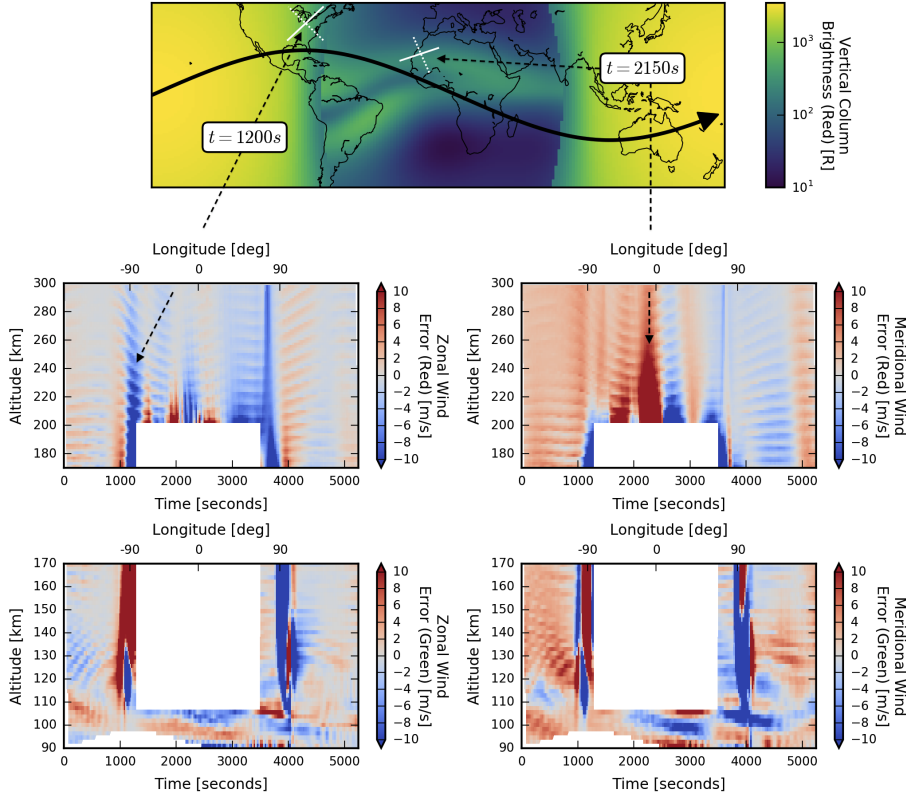


**Fig. 5** Result of the verification simulation without noise. (Top) A depiction of the simulated ICON orbit in black, overlaid on a map of the total vertical column brightness of the simulated red emission, for reference. For two example retrievals at  $t = 1200s$  and  $t = 2150s$ , the lines of sight of MIGHTI A and B are shown in white. (Bottom) The retrieval errors for the zonal and meridional wind and the red and green emissions are shown as a function of altitude and time, following ICON’s orbit. The two example retrievals are representative of the largest sources of error: spherical asymmetry near the terminator and the edge of the equatorial ionization anomaly.)

large. In practice, we plan to flag profiles when significant spherical asymmetry is suspected by comparing the brightness measurements from MIGHTI A and B. When they disagree, it is likely that variations along the line of sight are the cause. Large errors are also seen near  $0^\circ$  longitude in the red retrieval. These are also due to spherical asymmetry; they occur when the line of sight of MIGHTI crosses the edge of the equatorial ionization anomaly, where large horizontal gradients in the wind and emission rate exist. We will flag these profiles with the same algorithm.

#### 4.1.1 Vertical Resolution

In addition to errors arising from the presence of spherical asymmetries in the wind and airglow that violate the *ab initio* assumptions of this retrieval, there are sometimes significant errors arising from the limited vertical resolution of MIGHTI.

This is especially true for the green retrieval, which samples a region that can have larger wind shears [10] and vertical airglow gradients, which are not fully captured by the  $\sim 2.5$ -km altitude sampling. This has a potential impact on ICON's science objectives, since the observational geometry will tend to suppress the retrieved amplitude of tides with short vertical wavelengths.

To quantitatively assess this impact, we performed a simulation identical to the one described above, except that we used a wind profile that varies sinusoidally in altitude and is constant in latitude and longitude, shown in the left panel of Figure 6. This approximates an atmospheric tide, in that it has a horizontal scale larger than the line-of-sight integration path length, but a vertical scale for which the wind retrieval may be affected by the vertical sampling of the measurement. We fit the retrieved wind with a sinusoid to determine the retrieved amplitude error. Although we used a tide with an amplitude of 100 m/s, the results are invariant to amplitude, and we therefore show the results as a percentage.

This approach is useful because it characterizes the retrieval in the Fourier domain. Any wind profile can be decomposed into a sum of sinusoids, and since the retrieval is nearly linear, the retrieved wind profile is well approximated by the sum of the retrievals of the individual sinusoids. By using wind profiles with various vertical wavelengths, we characterize the ability of the inversion to retrieve various vertical scale sizes.

The right panel of Figure 6 summarizes the simulation results for various vertical wavelengths. We show results using the daytime green line airglow profile that is discussed in Section 4.2 and shown in Figure 7. The results are similar for other airglow profiles. For tides with vertical wavelengths as short as 10 km, the expected amplitude error introduced by the limited vertical resolution is 20%. For wavelengths larger than 30 km, the expected error is less than 5%. In cases where high vertical resolution is sought, such as a specialized retrieval of the large shear in the lower thermosphere, a higher-order summation rule can be used to convert the integral in (4) to the summation in (5); the default order is zero (i.e., Riemann-sum rule). Higher orders improve accuracy at the cost of precision. An accuracy vs. precision trade study can be performed with early flight data to optimize the algorithm used for the default Level 2 data product.

## 4.2 Precision

The precision of the retrieved wind depends strongly on the volume emission rate, which can vary dramatically. In order to predict performance, we use volume emission rate profiles generated from the models described above, averaged over latitudes, longitudes, and local times observed by MIGHTI, and over geophysical conditions during the 2009 solar minimum period, which is assumed to be representative of the conditions ICON will experience. These profiles are shown in Figure 7.

We simulate MIGHTI data products resulting from these profiles using the same approach described above. After simulating a 60-second exposure, we add shot, read, and dark noise to the raw Level 0 images based upon as-built instrument performance (see the right column of Table 3 of [4]; where MIGHTI A and B have different performance, we use the worst case). To improve statistics at the cost of resolution, we also bin (i.e., downsample) the raw images to the required altitude

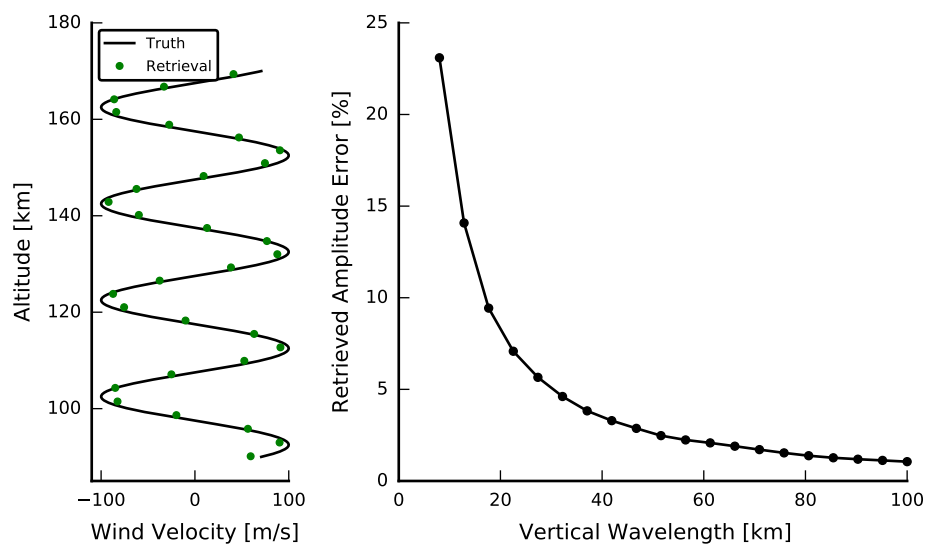


**Fig. 6** (Left) An example retrieval to test the effect of the limited 2.5-km vertical sampling. (Right) A summary of the ability to retrieve various vertical scale sizes.

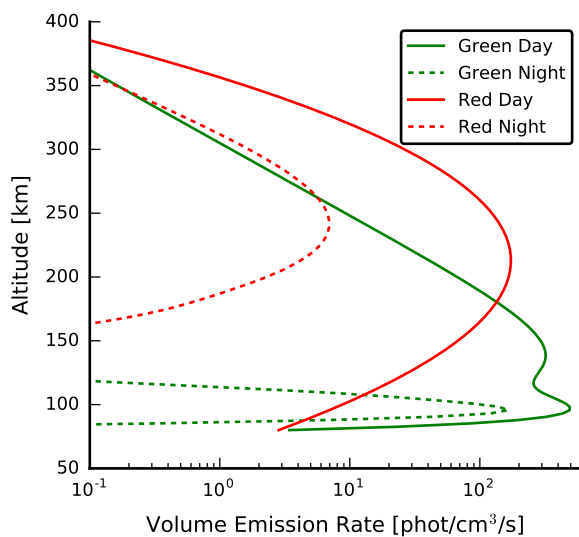


**Fig. 7** Representative solar-minimum airglow volume emission rate profiles used for the precision analysis.

sampling: 30 km for red and 5 km for green. To estimate the wind precision, we use a Monte Carlo simulation ( $N = 500$ ). Precision values represent 1-sigma uncertainties. To account for uncertainty in spacecraft pointing, we add 1 m/s in quadrature. Results are shown in Figure 8 and are compared to the L2 mission

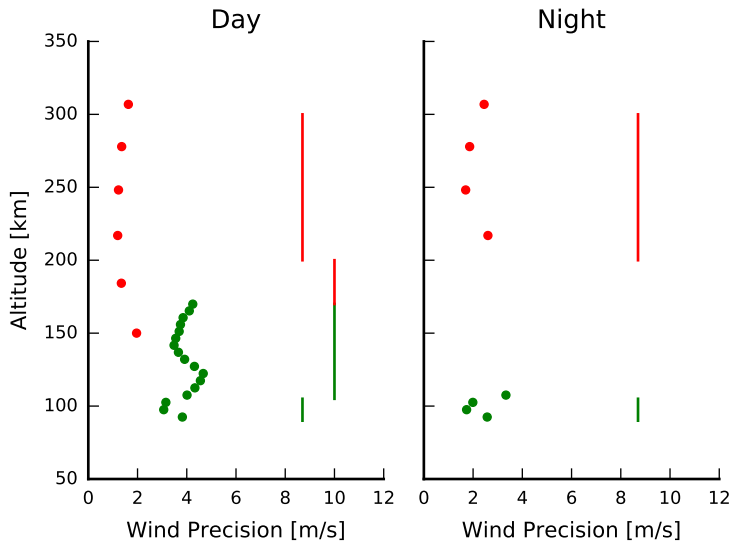


**Fig. 8** Precision of the MIGHTI wind product using as-built instrument parameters and average emission rate profiles, as described in the text. Red and green dots represent the precision of the red and green profiles, binned to 30-km and 5-km altitude resolution, respectively. Lines show the precision requirement. Shot noise, read noise, dark noise, and pointing uncertainty are included.

requirement, which is 8.7 m/s in the regions of 90-105 km and 200-300 km, with an additional daytime-only requirement of 10 m/s in the region of 105-200 km [9, 4]. At all altitudes, the precision prediction meets the requirement, ranging from 1.2 to 4.7 m/s.

## 5 Conclusion

This paper presents the thermospheric wind retrieval algorithm for MIGHTI, two interferometers on NASA’s ICON mission. MIGHTI measures interferometric limb images of the red and green airglow emissions. After removal of instrument artifacts, the first step of the retrieval applies an inversion to the interferograms to retrieve altitude profiles of the line-of-sight wind. The second step combines profiles from MIGHTI A and B to retrieve profiles of the vector horizontal wind. We have verified this algorithm with a simulation which tests its accuracy and precision. The dominant factor leading to loss of accuracy is horizontal variation of the wind and airglow emission rate, which are smoothed by the long path length of MIGHTI’s line of sight through the atmosphere. This error, which is common to all limb imagers, is nominally less than 10 m/s, except near the day/night boundaries and occasionally near the equatorial ionization anomaly, where severe violations of spherical symmetry render the data challenging to interpret. A secondary source of error is the vertical resolution, which limits the recovery of large shears that might be present in the lower thermosphere. The predicted precision of the wind retrieval meets requirements, as determined by an analysis using average solar

minimum emission rate profiles and as-built instrument performance. Precision depends strongly on the volume emission rate, which can vary by as much as two orders of magnitude.

Future work includes potentially coupling the Level 2.1 and Level 2.2 algorithms to estimate the vector horizontal wind directly. This may offer the ability to account for horizontal variations in the direction of the spacecraft velocity, but variations perpendicular to the spacecraft velocity cannot be resolved.

**Acknowledgements** B.J.H. was supported by the National Science Foundation Graduate Research Fellowship under Grant No. DGE-1144245. ICON is supported by NASA's Explorers Program through contracts NNG12FA45C and NNG12FA42I. This work uses pyglow, a Python package that wraps several upper atmosphere climatological models. The pyglow package is open-sourced and available at <https://github.com/timduly4/pyglow/>. The authors thank the ICON team for helpful comments. The primary contact for the ICON MIGHTI Level 2 wind products is Jonathan J. Makela ([jmakela@illinois.edu](mailto:jmakela@illinois.edu)).

## References

1. Barth, C.A.: Three-body reactions. *Annales de Geophysique* **20**, 182 (1964)
2. Bilitza, D., Reinisch, B.W.: International Reference Ionosphere 2007: Improvements and new parameters. *Advances in Space Research* **42**(4), 599–609 (2008). DOI [10.1016/j.asr.2007.07.048](https://doi.org/10.1016/j.asr.2007.07.048)
3. Englert, C.R., Babcock, D.D., Harlander, J.M.: Doppler asymmetric spatial heterodyne spectroscopy (DASH): concept and experimental demonstration. *Applied optics* **46**(29), 7297–307 (2007). URL <http://www.ncbi.nlm.nih.gov/pubmed/17932544>
4. Englert, C.R., Harlander, J.M., Brown, C.M., Marr, K.D., Miller, I., Stump, J.E., Hancock, J., Peterson, J., Kumler, J., Morrow, W., Mooney, T., Ellis, S., Mende, S., Harris, S.E., Stevens, M.H., Makela, J.J., Harding, B.J., Immel, T.J.: Michelson Interferometer for Global High-resolution Thermospheric Imaging (MIGHTI): Instrument Design and Calibration. *Space Science Reviews* **this issue** (2016)
5. Englert, C.R., Stevens, M.H., Siskind, D.E., Harlander, J.M., Roesler, F.L.: Spatial Heterodyne Imager for Mesospheric Radicals on STPSat-1. *Journal of Geophysical Research* **115**(D20), D20,306 (2010). DOI [10.1029/2010JD014398](https://doi.org/10.1029/2010JD014398). URL <http://doi.wiley.com/10.1029/2010JD014398>
6. Gault, W., Thuillier, G., Shepherd, G.: Validation of O (1S) wind measurements by WINDII: the WIND Imaging Interferometer on UARS. *Journal of geophysical research* **101** (1996). URL <http://www.agu.org/pubs/crossref/1996/95JD03352.shtml>
7. Hernandez, G.: Lower-thermosphere temperatures determined from the line profiles of the O I 17,924-K (5577 Å) emission in the night sky, 1. Long-term behavior. *Journal of Geophysical Research* **81**(28), 5165–5172 (1976). DOI [10.1029/JA081i028p05165](https://doi.org/10.1029/JA081i028p05165). URL <http://doi.wiley.com/10.1029/JA081i028p05165>
8. Hernandez, G., Roble, R.G.: Direct measurements of nighttime thermospheric winds and temperatures, 2. Geomagnetic storms. *Journal of Geophysical Research* **81**(28), 5173–5181 (1976). DOI [10.1029/JA081i028p05173](https://doi.org/10.1029/JA081i028p05173). URL <http://doi.wiley.com/10.1029/JA081i028p05173>
9. Immel, T., England, S.L., Mende, S.B., Heelis, R.A., Englert, C.R., Edelstein, J., Frey, H.U., Taylor, E.R., Craig, W.W., Bust, G.S., Crowley, G., Forbes, J.M., Gerard, J.C., Harlander, J.M., Huba, J.D., Hubert, B., Kamalabadi, F., Makela, J.J., Maute, A.I., Meier, R.R., Raftery, C., Rochus, P., Siegmund, O.H.W., Stephan, A.W., Swenson, G.R., Frey, S., Hysell, D.L., Saito, A.: The Ionospheric Connection Explorer Mission: Mission Goals and Design. *Space Science Reviews* **this issue** (2016)
10. Larsen, M.F.: Winds and shears in the mesosphere and lower thermosphere: Results from four decades of chemical release wind measurements. *Journal of Geophysical Research* **107**(A8), 1215 (2002). DOI [10.1029/2001JA000218](https://doi.org/10.1029/2001JA000218). URL <http://doi.wiley.com/10.1029/2001JA000218>

11. Link, R., Cogger, L.L.: A reexamination of the O I 6300-Å nightglow. *Journal of Geophysical Research* **93**(A9), 9883 (1988). DOI 10.1029/JA093iA09p09883. URL <http://doi.wiley.com/10.1029/JA093iA09p09883>
12. Link, R., Cogger, L.L.: Correction to "A reexamination of the O I 6300-Å nightglow" by R. Link and L. L. Cogger. *Journal of Geophysical Research* **94**(A2), 1556 (1989). DOI 10.1029/JA094iA02p01556. URL <http://doi.wiley.com/10.1029/JA094iA02p01556>
13. McDade, I.C., Murtagh, D., Greer, R., Dickinson, P., Witt, G., Stegman, J., Llewellyn, E., Thomas, L., Jenkins, D.: ETON 2: Quenching parameters for the proposed precursors of O<sub>2</sub>(b<sup>1</sup>Σ<sub>g</sub><sup>+</sup>) and O(1S) in the terrestrial nightglow. *Planetary and Space Science* **34**(9), 789–800 (1986). DOI 10.1016/0032-0633(86)90075-9. URL <http://linkinghub.elsevier.com/retrieve/pii/0032063386900759>
14. Menke, W.: *Geophysical Data Analysis: Discrete Inverse Theory*. International Geophysics. Elsevier Science (1989). URL <http://books.google.com/books?id=NvKx-bWJsyUC>
15. Murtagh, D., Witt, G., Stegman, J., McDade, I., Llewellyn, E., Harris, F., Greer, R.: An assessment of proposed O(1S) and O<sub>2</sub>(b<sup>1</sup>Σ<sub>g</sub><sup>+</sup>) nightglow excitation parameters. *Planetary and Space Science* **38**(1), 43–53 (1990). DOI 10.1016/0032-0633(90)90004-A. URL <http://linkinghub.elsevier.com/retrieve/pii/003206339090004A>
16. Picone, J.M., Hedin, A.E., Drob, D.P., Aikin, A.C.: NRLMSISE-00 empirical model of the atmosphere: Statistical comparisons and scientific issues. *Journal of Geophysical Research: Space Physics* **107**(A12), 1–16 (2002). DOI 10.1029/2002JA009430
17. Roble, R.G.: The NCAR thermosphere-ionosphere-mesosphere-electrodynamics general circulation model (TIME-GCM). In: R. Schunk (ed.) *STEP Handbook on Ionospheric Models*, pp. 281–288. Utah State Univ., Logan (1996)
18. Roble, R.G., Ridley, E.C.: A thermosphere-ionosphere-mesosphere-electrodynamics general circulation model (time-GCM): Equinox solar cycle minimum simulations (30–500 km). *Geophysical Research Letters* **21**(6), 417–420 (1994). DOI 10.1029/93GL03391. URL <http://doi.wiley.com/10.1029/93GL03391>
19. Rochon, Y.J.: The Retrieval of Winds, Doppler Temperatures, and Emission Rates for the WINDII Experiment. Ph.D. thesis, York University (2000). URL <http://www.collectionscanada.gc.ca/obj/s4/f2/dsk2/ftp03/NQ56265.pdf>
20. Shepherd, G., Thuillier, G.: WINDII, the wind imaging interferometer on the Upper Atmosphere Research Satellite. *Journal of Geophysical Research* **98**(2) (1993). URL <http://onlinelibrary.wiley.com/doi/10.1029/93JD00227/full>
21. Shepherd, G.G., Thuillier, G., Cho, Y.M., Duboin, M.L., Evans, W.F.J., Gault, W.A., Hersom, C., Kendall, D.J.W., Lathuillière, C., Lowe, R.P., McDade, I.C., Rochon, Y.J., Shepherd, M.G., Solheim, B.H., Wang, D.Y., Ward, W.E.: The Wind Imaging Interferometer (WINDII) on the Upper Atmosphere Research Satellite: A 20 year perspective. *Reviews of Geophysics* **50**(2), RG2007 (2012). DOI 10.1029/2012RG000390. URL <http://doi.wiley.com/10.1029/2012RG000390>
22. Stevens, M.H., Englert, C.R., Marr, K.D., Harlander, J., England, S.L., Immel, T.J.: The Retrieval of Lower Thermospheric Temperatures Using MIGHTI Observations of the O<sub>2</sub> A Band. *Space Science Reviews* **this issue** (2016)
23. Vargas, F., Swenson, G., Liu, A., Gobbi, D.: O( 1 S), OH, and O 2 (b) airglow layer perturbations due to AGWs and their implied effects on the atmosphere. *Journal of Geophysical Research* **112**(D14), 1–11 (2007). DOI 10.1029/2006JD007642. URL <http://doi.wiley.com/10.1029/2006JD007642>  
<http://www.agu.org/pubs/crossref/2007/2006JD007642.shtml>
24. Zhang, S.P., Shepherd, G.G.: On the response of the atomic oxygen red line emission rates to the Sun's energy input: an empirical model deduced from WINDII/UARS global measurements. In: *Proc. SPIE*, vol. 5979, pp. 597,912–597,912–10 (2005). DOI 10.1117/12.627150. URL <http://proceedings.spiedigitallibrary.org/proceeding.aspx?articleid=1333031>
25. Zhang, S.P., Shepherd, G.G.: On the response of the O( 1 S) dayglow emission rate to the Sun's energy input: An empirical model deduced from WINDII/UARS global measurements. *Journal of Geophysical Research* **110**(A3), A03,304 (2005). DOI 10.1029/2004JA010887. URL <http://doi.wiley.com/10.1029/2004JA010887>